Geophys. J. Int. (DOI: 10.1093/gji/ggx502)

Role of geometric barriers in irregular-rupture evolution during the 2008 Wenchuan earthquake

R. Okuwaki[1], Y. Yagi[2]

[1] *Graduate School of Life and Environmental Sciences, University of Tsukuba, Tsukuba 305-8572, Japan.*

[2] *Faculty of Life and Environmental Sciences, University of Tsukuba, Tsukuba 305-8572, Japan.*

SUMMARY

Geometric discontinuities within fault systems known as geometric barriers contribute to irregular rupture evolutions during earthquakes. We applied a hybrid backprojection method to high-frequency teleseismic P-waveforms to investigate the role of geometric barriers in the rupture propagation during the M_{W} 7.9 2008 Wenchuan, Chine, earthquake. We found that sources of high-frequency waves were concentrated near the intersections of a northwest-trending cross-cutting fault with the dominant northeast-trending fault system and in areas around steps between fault segments of the dominant fault system. We recognized these areas as geometric barriers to rupture propagation. Our analysis of the high-frequency waves associated with the geometric discontinuities within the fault system showed that geometric barriers can decelerate or stop rupture propagation, but can also accelerate rupture when the rupture front crosses a geometric barrier and instigates rupture in an adjacent fault segment. Our result suggests that geometric discontinuities within fault systems can cause earthquake rupture propagation that is more complex than that of faults of simpler geometry associated with subduction zone megathrust earthquakes.

Key words: Image processing; Time-series analysis; Earthquake dynamics; Earthquake hazards; Earthquake source observations

1 INTRODUCTION

An earthquake fault, in nature, has a geometric complexity in a wide scale range (Aki 1979; King & Nábělek 1985; Wesnousky 2008), including kinks, steps, and jogs that can cause irregularities in rupture propagation when the rupture front reaches localized areas where the strength of the materials is greater than the regional tectonic stress, and/or due to the dynamic disturbance of stress (Aki 1979; Das & Aki 1977; Kase & Day 2006). Such irregularities are expressed as abrupt changes of slip rate and/or rupture-front velocity and have been shown by earthquake fault modeling to enhance the radiation of high-frequency waves (Madariaga 1977; Bernard & Madariaga 1984; Spudich & Frazer 1984; Madariaga et al. 2006). From where and how the high-frequency waves are radiated are the critical concerns for both earthquake seismologists and engineers since the resonant frequencies of buildings lie in the frequency band for such high-frequency waves (Clinton 2006; Snieder & Şafak 2006; Kohler et al. 2007). In particular, many earthquakes in densely populated inland areas have been associated with geometrically complex fault systems (Sekiguchi 2000; Wright et al. 2001; Michel & Avouac 2002; Xu et al. 2009a), so evaluation of the production of high-frequency waves along these fault systems may provide valuable information about rupture evolution that can be used to mitigate future earthquake disasters in populous inland areas.

In 1990s, pioneering studies of observing high-frequency wave radiation sources have been archived by development of envelope inversion methods (e.g. Gusev & Pavlov 1991; Zeng et al. 1993; Cocco & Boatwright 1993; Kakehi & Irikura 1996; Nakahara et al. 1998). The envelope inversion has drawn the fruitful knowledge of the source process during the earthquake, for example, Kakehi et al. (1996) has shown that the high-frequency radiation sources were identified at the fault step-over during the 1995 Kobe, Japan, earthquake, suggesting that the step over behaved as geometric barrier that could generate the high-frequency waves. Zeng et al. (1993) and Kakehi & Irikura (1996) have also presented the complementary distributions of the high-frequency radiation sources and the slip distribution obtained by conventional waveform inversion using the low-frequency-filtered waveforms. However, as reviewed in detail by Nakahara (2008), this complementarity is not always true, which may partly be resulted from the insufficient spatial resolution of the envelope inversion (e.g. Kakehi & Irikura 1997).

Following the developments of the envelope inversion, Backprojection (BP) techniques were first applied to the great 2004 Sumatra-Andaman earthquake (Krüger & Ohrnberger 2005; Ishii et al. 2005), and have since made it possible to track sources of the high-frequency waves. Further developments of BP techniques have uncovered the hidden-rupture images of earthquake rupture that had previously been difficult to resolve by the kinematic waveform inversion alone, for example, multiple branching ruptures (Meng et al. 2012b; Fan et al. 2016, 2017) and triggering mechanisms of asperity ruptures (Allmann & Shearer 2007; Okuwaki et al. 2014; Yagi & Okuwaki 2015; Okuwaki et al. 2016). En-

hancement of the spatial resolution of the projected image by adopting the global stations with good azimuthal coverage (Walker et al. 2005; Allmann & Shearer 2007; Yagi et al. 2012a; Okuwaki et al. 2014; Fan & Shearer 2015) is another advance for the observation of high-frequency wave radiation. Relationship between rupture evolution captured via analyses of high-frequency waveforms based on the BP techniques and the geometric complexity of a fault system has been discussed in the pioneering studies (e.g. Uchide et al. 2013). However due to the poor depth resolution of the BP image (e.g. Xu et al. 2009b), it has been difficult to image sources of high-frequency waves that are possibly extending to deeper parts of faults. Besides, the spatiotemporal change of the focal mechanism, related to the geometric complexity in the fault system, is not explicitly taken into account by the BP method, and may not be well resolved enough to discuss in detail the role of geometric discontinuity within the fault system. The Hybrid BP (HBP) method (Yagi et al. 2012a; Okuwaki et al. 2014) ensures better resolution at depth by using the differences of travel times and phase amplitudes between the P-phase and depth phases (pP and sP), extracted by cross correlation of observed waveforms with the theoretically calculated Greens functions. An explicit use of the Greens functions allows us to assume fault geometry, and the HBP method can then be used to assess how fault geometry is related to the emission of high-frequency waves, or to irregular rupture propagation.

Detailed geological surveys and analyses of geodetic data after the 12 May 2008 Wenchuan earthquake (M_{W} 7.9) in China, including Global Positioning System (GPS) and interferometric synthetic aperture radar (InSAR) data, revealed clear surface ruptures indicating that rupture propagated along a multi-segment fault system characterized by kinks, steps, and sub-parallel faults (Xu et al. 2009a; Hashimoto et al. 2010; Fielding et al. 2013; Wan et al. 2017) (Fig. 1). Thus, the 2008 Wenchuan earthquake provides an opportunity to investigate the relationship between the geometric complexity of a fault system and irregular rupture propagation by analysis of high-frequency waveforms. The surface ruptures of the 2008 Wenchuan earthquake generally trend northeast along the Longmen Shan thrust belt, which lies along the eastern margin of the Tibetan Plateau in an area where the elevation of the land rises steeply westward from 500 m to more than 4000 m above the Sichuan basin (Burchfiel et al. 2008). Analyses of the focal mechanisms of relocated aftershocks and seismic reflection data have shown that the dips of the faults steepen from southwest to northeast of the epicentre (Yu et al. 2010; Hubbard & Shaw 2009; Hubbard et al. 2010). A notable feature of the fault system is that both the southern Beichuan fault (SBF) segment and the sub-parallel Pengguan segment are cut by the Xiaoyudong fault (XDF), a small, vertical tear fault that strikes roughly perpendicular to the Beichuan and Pengguan fault segments (Liu-Zeng et al. 2012) and corresponds spatially with kinks in both of them (Fig. 1). The XDF has attracted the attention of seismologists because of its possible role in irregular rupture propagation along the fault system (e.g. Hartzell et al. 2013).

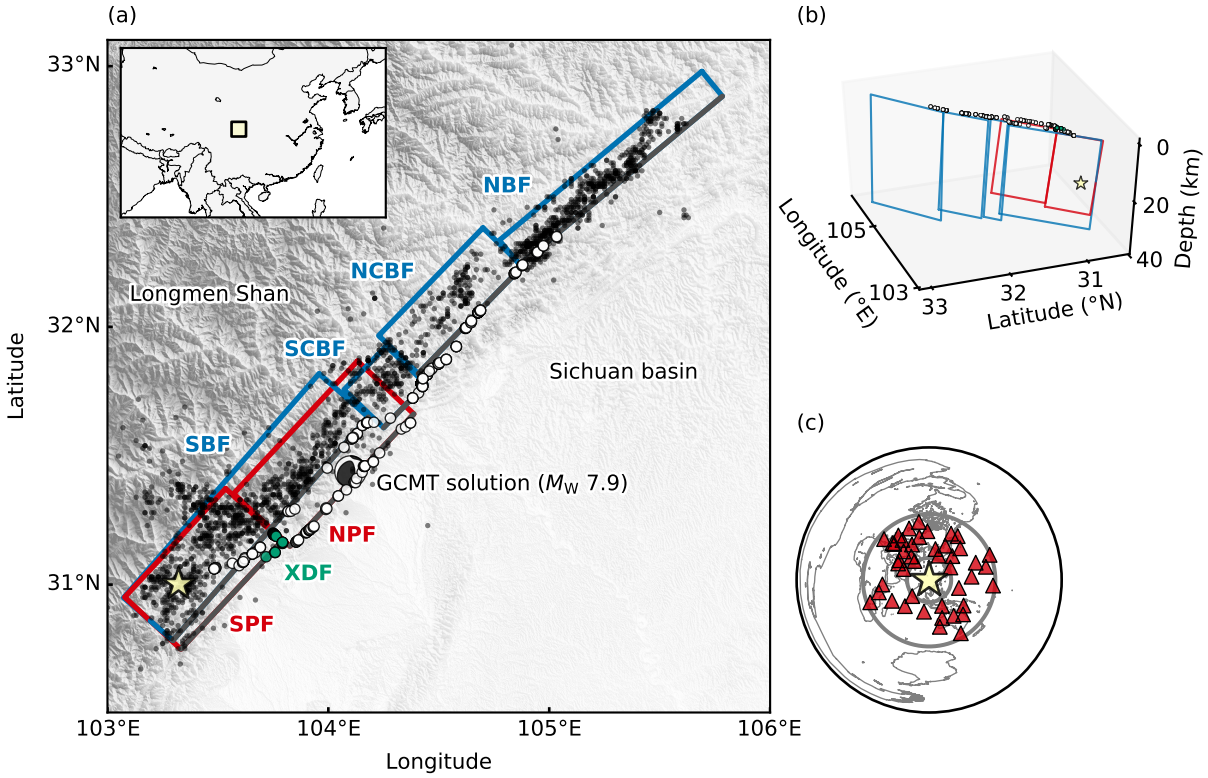

Figure 1. Overview of the source region of the 2008 Wenchuan earthquake and fault model, and distribution of seismic stations used in this study. (a) Map showing the epicentre (star), the relocated aftershocks (black dots) (Yu et al. 2010), the Global Centroid Moment Tensor solution (beach ball; http://www.globalcmt.org, last accessed on August 12, 2017), locations of surface ruptures along the Beichuan-Pengguan segments (white circles) and the XDF (green circles) (Xu et al. 2009a), and the presumed fault segments used in the fault model of this study (blue and red rectangles representing the Beichuan and Pengguan fault segments, respectively, accompanied with their fault segment names of SBF, south Beichuan fault; SCBF, south-central Beichuan fault; NCBF, north-central Beichuan fault; NBF, north Beichuan fault; SPF, south Pengguan fault; and NPF, north Pengguan fault). Gray lines represent the shallowest edge of each fault segment. Background topography is derived from 2010 Global Multi-resolution Terrain Elevation Data 7.5-arcsecond spaced mean elevations (Danielson & Gesch 2011). Inset map shows the location of the study area (yellow shaded box). (b) Three-dimensional view of presumed fault geometry (blue and red rectangles, representing the Beichuan and Pengguan fault segments, respectively) projected from 290° azimuth and 40° elevation, also showing the hypocentre (star) and locations of surface ruptures along the Beichuan-Pengguan segments (white circles) and the XDF (green circles) (Xu et al. 2009a). (c) Distribution of teleseismic stations used in this study (triangles). The star marks the epicentre, and the two gray circles represent epicentral distances of 30° and 90°.

Table 1. Geometric parameters for each fault segment.

Segment	Strike (°)	Dip (°)	Length (km)	Width (km)
SBF	221	45	130	42
SCBF	224	54	28	42
NCBF	224	54	66	42
NBF	230	70	114	42
SPF	223	34	66	42
NPF	223	34	80	42

Various patterns of coseismic slip during the 2008 Wenchuan earthquake have been proposed on the basis of numerous seismic source models constructed by solely or jointly inverting seismic waveforms recorded at teleseismic or near-field distances, GPS data, and InSAR data (Shen et al. 2009; Yagi et al. 2012b; Fielding et al. 2013; Hartzell et al. 2013); the common knowledge drawn from these studies is that rupture propagated almost exclusively to the northeast, that there were several patches of larger slip, and that slip motions generally rotated from reverse faulting to right-lateral faulting as the rupture front propagated northeast from the epicentre. BP studies using high-frequency ($\sim$1 Hz) teleseismic P-waveforms (Xu et al. 2009b; Zhang & Ge 2010) have shown that rupture propagated almost entirely to the northeast at speeds of 2.8–3.0 km/s. These results are consistent with inverted slip models based on low-frequency waveforms and indicate that there were several bursts of high-frequency waves that coincide with areas where there was severe damage (Xu et al. 2009b). However, because the BP images were projected only at the surface, and resolution in the dip direction was poor, there is still room for evaluations of the radiation of high-frequency waves in the context of complex fault geometry.

Here we present our estimates of the spatiotemporal distribution of high-frequency wave radiators by using globally observed teleseismic P-waveforms of the 2008 Wenchuan earthquake and discuss the role of geometric barriers in irregular rupture propagation along the fault system.

2 FAULT MODEL

We modeled the possible source regions on the sub-parallel Beichuan and Pengguan faults by using seven rectangular fault segments composed of discretized source nodes on 2 km (strike) $\times$ 2 km (dip) grids (Fig. 1 and Table 1). Each fault segment was placed according to surface traces of ruptures mapped during filed surveys (Xu et al. 2009a) and the geodetic measurements of the

SAR pixel offsets (Fielding et al. 2013). Our selections of the dip angle and depth-extent for each fault segment were guided by the focal mechanisms of the relocated aftershocks (Yu et al. 2010) and a three-dimensional fault model constructed from seismic reflection and surface geological data (Hubbard & Shaw 2009; Hubbard et al. 2010). We considered non-uniqueness of the assumptions of the fault model by using the single monoplane fault model (Supporting Information Fig. S1) and confirmed that the arbitrariness of the geometrical model we used did not affect our results. We did not include the XDF in the fault model because its length ($\sim$7 km) (Liu-Zeng et al. 2012) is similar to the spatial resolution of the HBP method for high-frequency waveforms (Supporting Information Fig. S2 for synthetic-resolution tests of the HBP method). We adopted the epicentre (31.002°N, 103.32°E) determined by the U.S. Geological Survey, National Earthquake Information Center (https://earthquake.usgs.gov/earthquakes/eventpage/usp000g650, last accessed on August 12, 2017). The hypocentral depth was assumed to be on 15 km depth at the intersection of the SBF and the south Pengguan fault (SPF) segments.

3 DATA PROCESSING

We downloaded 44 vertical-component P-waveforms of the 2008 Wenchuan earthquake, recorded at the Global Seismograph Network (GSN) stations at teleseismic distances (between 30° and 90°) via the Incorporated Research Institutions for Seismology Data Management Center (IRISDMC; Fig. 1c). We selected the data to ensure good azimuthal coverage and sufficient signal to noise ratio. The first arrival of the P-phase on each waveform was manually picked, and the instrumental response was deconvolved to velocity at a sampling rate of 0.05 s.

We then estimated the spatiotemporal distributions of sources of high- and low-frequency waves by solving the following three equations:

$$c_{ij}(t,\phi_k,\delta_k,\lambda_k) = \frac{u_j(t)\hat{\times}G_{ij}(t,\phi_k,\delta_k,\lambda_k)}{\sqrt{\int u_j^2(t)dt}\cdot\sqrt{\int G_{ij}^2(t,\phi_k,\delta_k,\lambda_k)dt}}, \tag{1}$$

$$r_i(t,\phi_k,\delta_k,\lambda_k) = \sum_j a_j|c_{ij}|^{\frac{1}{N}}\cdot\frac{c_{ij}}{|c_{ij}|}(t,\phi_k,\delta_k,\lambda_k), \tag{2}$$

$$s_i(t) = \max_k|r_i|^N\cdot\frac{r_i}{|r_i|}(t,\phi_k,\delta_k,\lambda_k). \tag{3}$$

First, we calculated the normalized cross correlation function c_{ij} of the observed waveform u_j at jth station and the corresponding Green's function G_{ij} for each pair of jth station and ith source node (eq. 1). r_i is then calculated by stacking N-th root of the c_{ij} for all the stations by preserving each sign of c_{ij}, where a_j is a controlling factor to prevent possible bias due to the station distribution (eq. 2). In this study, we introduced components of focal mechanism k (strike ϕ_k, dip δ_k, and rake λ_k,

defined by Aki & Richards (2002)) on each source node for calculating Green's functions, and we finally obtained the signal intensity s_i at each source node that maximizes N-th power of r_i among the components of focal mechanism (eq. 3). Note that strike and dip angles were fixed for each fault segment (Table 1), and the range of rake angle, between 0°and 180°with an increment of 5°, was constrained by geological surveys of the surface ruptures, which show that the reverse faulting is dominant in the vertical off-sets (Xu et al. 2009a; Yu et al. 2010). Eqs. (2) and (3) represent the N-th root stacking ($N = 4$) (Muirhead & Datt 1976) to enhance the signal to noise ratio of the c_{ij}. Green's functions were computed based on the method of Kikuchi & Kanamori (1991). The travel times, the geometrical spreading factors, and the ray parameters were calculated with the ak135 model (Kennett et al. 1995), and the CRUST1.0 model (Laske et al. 2013) was used to construct the near-source structure (Supporting Information Table S1) for calculation of the Haskell propagator matrix in the Greens function. High-frequency (0.5–2.0 Hz) and low-frequency (0.1–0.5 Hz) Butterworth bandpass filters were applied to both the observed waveforms and the Greens functions before cross correlation for the high- and low-frequency analyses, respectively.

4 SOURCES OF HIGH-FREQUENCY WAVES

Our analysis showed that sources of high-frequency (0.5–2.0 Hz) waves with strong signal intensity were concentrated near geometric discontinuities of the fault system where the XDF cuts the middle part of the SBF (∼70 km along strike), and where it crosses near the boundary between the SPF and the north Pengguan fault (NPF) segments at 5–10 km depth at 15–25 s from the hypocentral time (Figs. 2a, 3a and Supporting Information S3a). Other sources of high-frequency waves of modest intensity were observed at the northeastern edge of the NPF and at the boundaries between the SBF and the south-central Beichuan fault (SCBF) segments, and between the SCBF and the north-central Beichuan fault (NCBF) at 50–60 s from the hypocentral time (Figs. 2a and 3a). Under the assumption that the high-frequency P-waves were radiated from the rupture front, the rupture-front velocity from the epicentre along the strike of the SBF (221°) was 2–3 km/s (Fig. 3a). Although the gross trend of rupture propagation was to the northeast, for the first ∼10 s after the hypocentral time, high-frequency sources of modest intensity appeared southwest of the epicentre along both the SBF and the SPF (Fig. 3a), suggesting that there was also some early southwestward rupture propagation. The high-frequency sources of modest intensity on the SPF also migrated southwestward after the strong bursts of high-frequency waves near its intersection with the XDF. The rake angles that contributed most to the radiation of high-frequency waves at each source node were scattered (Fig. 2a), making it difficult to retrieve a representative direction of slip motion from the high-frequency analysis.

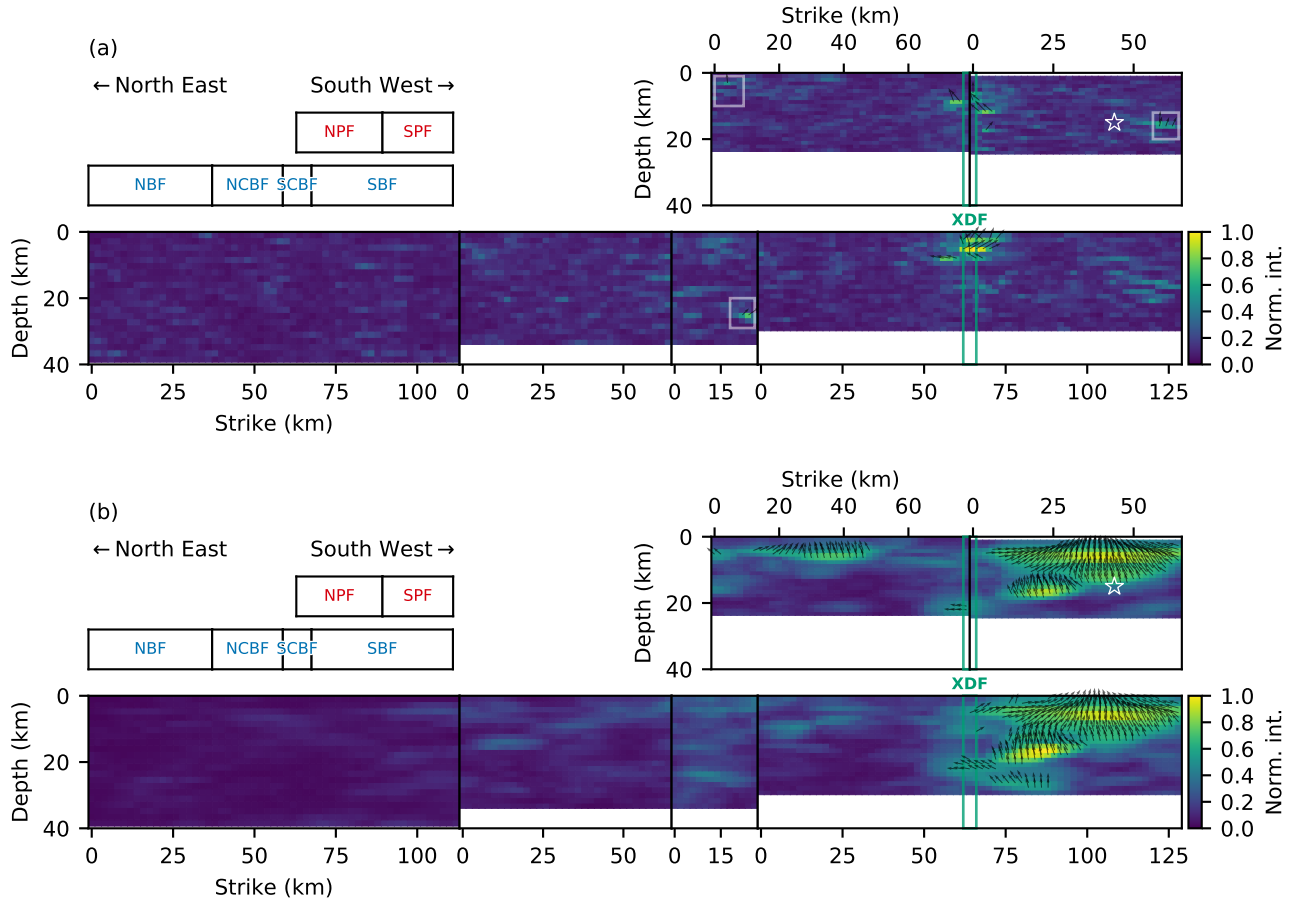

Figure 2. High- and low-frequency wave sources. (a) Spatial distribution of high-frequency sources in a strike vs. depth view. Background colors represent normalized signal intensities. Arrows show rake angles, which for clarity are shown only on source cells for which signal intensities are greater than 0.5. White rectangles represent the locations of modest intensity of high-frequency sources. Green lines indicate the estimated location of the XDF and the star marks the hypocentre. (b) Same as Fig. 2a, but for the low-frequency result. Configuration of the fault segments is summarized at top-left corner on each panel. See caption of Fig. 1a for fault segment names.

5 SOURCES OF LOW-FREQUENCY WAVES

We estimated the locations of sources of low-frequency (0.1–0.5 Hz) waves as we did for the high-frequency waveforms (Figs. 2b, 3b and Supporting Information Fig. S3b). In contrast to the sources of high-frequency waves, sources of strong intensity of low-frequency waves were around the middle parts of both the SBF and the SPF, rather than near geometric discontinuities of the fault system. The spatial resolution of the low-frequency result is generally inferior to that of the high-frequency result (Supporting Information Fig. S2), and the spatial distance of some of the presumed fault segments are

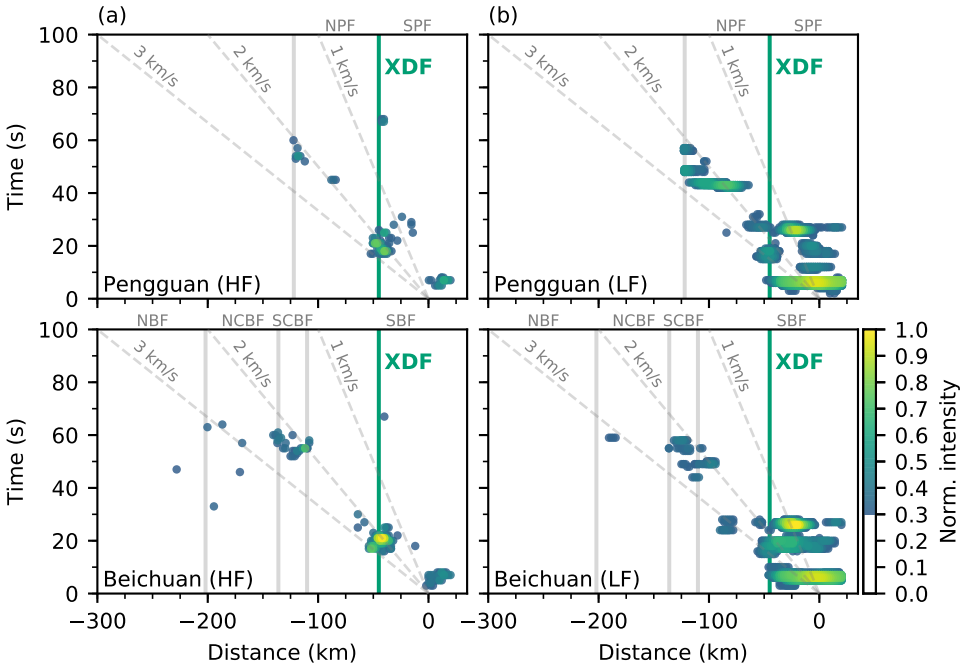

Figure 3. Spatiotemporal distribution of sources of high- and low-frequency waves. (a) Colored circles indicate the spatiotemporal distribution of locations of high-frequency (HF) signals along the Pengguan fault segments (SPF and NPF; upper panel) and the Beichuan fault segments (SBF, SCBF, NCBF and NBF; lower panel). Color scheme is the same as in Fig. 2. For clarity, only sources of normalized intensity greater than 0.3 are shown. The abscissae are distances from the epicentre along the strike (221°) direction, and the ordinate is an elapsed time from the hypocentral time. The estimated locations of the XDF (green line) and reference rupture speeds (gray dashed lines) are also shown. Gray solid lines represent the segment boundaries. (b) Same as Fig. 3a, but for the low-frequency (LF) result.

within the spatial resolution of the HBP method for the low-frequency waveforms, the distributions of low-frequency sources on the sub-parallel SBF and SPF are similar, as are those of the SCBF and the northeastern edge of the NPF (Fig. 2b). The sources of low-frequency waves propagated mainly northeastward until ∼20 s after the hypocentral time, but thereafter they migrated bilaterally southwestward and northeastward from the XDF (Fig. 3b). The southwestward propagation quickly ceased ∼30 s after the hypocentral time, whereas the northeastward propagation continued until ∼50 s from the hypocentral time (Fig. 3b). Note that estimation of rupture velocity from the low-frequency data is difficult owing to its spatial resolution. The low-frequency result gave a smoother distribution of rake angles than did the high-frequency result (Fig. 2b). Reverse faulting is dominant for the southwestern part of the SBF and the middle part of the SPF, whereas right-lateral faulting is evident near the XDF.

6 DISCUSSIONS AND CONCLUSION

Analytical studies and numerical experiments of rupture propagation have shown that irregular-rupture propagation can enhance high-frequency wave radiations (Das & Aki 1977; Madariaga 1977; Bernard & Madariaga 1984; Spudich & Frazer 1984). Irregular rupture propagation occurs when rupture front encounters a barrier that stops or slows rupture propagation (Das & Aki 1977; Aki 1979). In particular, barriers in the form of geometric discontinuities of fault orientation or extent have been shown in numerical simulations to contribute to violations of rupture velocity (Kase & Day 2006; Oglesby 2008; Oglesby & Mai 2012; Madariaga et al. 2006).

Our analyses showed that the sources of high-frequency waves during the 2008 Wenchuan earthquake were concentrated mainly around the intersections of the XDF with other fault segments and at the steps across strike of faults at the northeastern edge of the NPF and at the boundaries between the SBF and the SCBF segments. Those areas have previously been recognized on the basis of surface ruptures as geometric barriers to rupture propagation during the 2008 Wenchuan earthquake (Xu et al. 2009a; Fielding et al. 2013). The radiation of high-frequency waves from these areas can be interpreted as a response to abrupt deceleration or acceleration of rupture-front propagation. The high-frequency sources on the SBF and SPF were temporarily arrested at their intersections with the XDF at 15–25 s from the hypocentral time, and then migrated bilaterally southwestward and northeastward from the XDF (Fig. 3a). We interpret this behavior to represent a deceleration of rupture when the rupture front encountered a discontinuity, followed by acceleration of rupture when the rupture front passed the barrier and recommenced propagation bilaterally away from the barrier through the adjacent fault segments. The deceleration of rupture that we inferred at the XDF on the basis of high-frequency data is consistent with a previous inverted coseismic slip model that showed a deficiency of coseismic slip or a suspension of rupture propagation near the XDF, 10–20 s after the hypocentral time (Yagi et al. 2012b). We also noted high-frequency signals of modest intensity at the southwestern ends of the SBF and the SPF during the very early stage of rupture ($\sim$10 s from the hypocentral time); these are consistent with coseismic slip modeling (Hartzell et al. 2013) that suggests southwestward propagation of slip along the Pengguan fault. Thus, we interpret these high-frequency signals to represent stopping phases (Madariaga 1977) of the initial southward propagation of rupture at the southwestern ends of the SPF and SBF. Bilateral-rupture propagation can also be seen in the SCBF at 50–60 s after the origin time (Fig. 3a), and the HF sources that are recognized at the boundaries of the SBF-SCBF and SCBF-NCBF and the northwestern edge of the NPF (Fig. 3a) can also be interpreted as the stopping phases or abrupt rupture decelerations.

If we consider the distribution of the maximum, median, and mean values of high- and low-frequency signal intensities along the dip directions of the fault segments (Fig. 4), we see that the

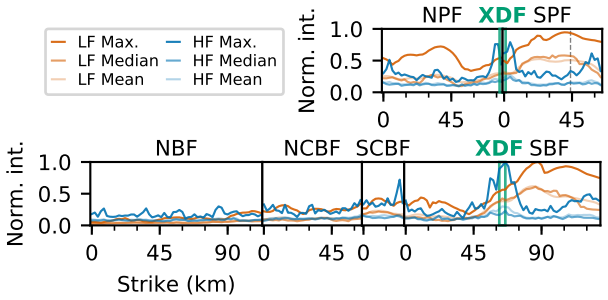

Figure 4. Distributions of maximum, median, and mean values of signal intensity along the dip direction of each fault segment (see Fig. 1a caption for fault segment names). The abscissae give distances along strike from the left-bottom corner of each fault segment, and the ordinate is a normalized signal intensity. Cold and warm colors represent the high- and low-frequency (HF and LF) results, respectively. The estimated locations of the XDF (green lines) and the location of the hypocentre (gray dotted line) are also shown.

distributions of sources of high- and low-frequency waves are roughly complementary in the southwestern segments (SBF, SCBF, SPF, and NPF); these distributions are consistent with the underlying theoretical framework, which predicts that propagation of a rupture front at constant speed does not contribute to high-frequency radiations (Spudich & Frazer 1984). Other studies have shown complementary relationship between the distribution of sources of high-frequency waves and zones of large slip (Meng et al. 2012a; Uchide et al. 2013; Okuwaki et al. 2014; Grandin et al. 2015; Yagi & Okuwaki 2015; Okuwaki et al. 2016). Thus, the distribution of sources of high-frequency waves should correspond to areas where rupture propagation is disturbed by geometric discontinuities within or between fault segments, whereas that of low-frequency waves should correspond to areas of smooth rupture propagation along the continuous and linear parts of fault segments. A seismic source model for the M_{W} 7.2 2010 El Mayor-Cucapah earthquake (Uchide et al. 2013) has a general similarity to our result, which also placed sources of high-frequency waves in areas near the boundaries of fault segments that can be interpreted to represent geometric barriers. While in the northeastern segments (NCBF and NBF) in Fig. 4, the relative intensities of high- and low-frequency signals are almost identical, and this may result from either the cases of that the signal intensity for both the high- and low-frequency waves are inherently weak compared to the ones in the southwestern segments, or that the intensities of both the HF and LF waves in the northeastern segments may be contaminated and weaken by the later phases of the main rupture along the southwestern segments. These effects may also explain the lack of the high-frequency radiation around the boundary between the NCBF and NBF, even though the geometric discontinuity is recognized in the surface ruptures and some amounts of slip are observed in the waveform inversion (e.g. Yagi et al. 2012b).

Geometric discontinuities are not generally characteristic of faults associated with subduction

zone earthquakes, but sources of high-frequency waves were identified at the edges of large asperity ruptures in studies combining the use of waveform inversion with an approach similar to ours (Okuwaki et al. 2014, 2016) concluded that for subduction zone earthquake a heterogeneous distribution of fracture energy or stress drop might release high-frequency waves when rupture propagation accelerates and triggers following large slip, which is consistent with the cascading rupture model (Ide & Aochi 2005). The above descriptions of the rupture propagation for the subduction zone earthquake on the basis of high-frequency data do not replicate the results of our analysis of the 2008 Wenchuan earthquake, where there are significant geometric discontinuities within the fault system. Our results suggest that if there are geometric discontinuities within a fault system, the characteristics of rupture propagation determined from teleseismic high-frequency waveforms is more complex than is the case for the generally simpler fault systems characteristic of subduction zone earthquakes; the high-frequency waves might be a consequence of abrupt deceleration or cessation of rupture propagation at a geometric discontinuity, or perhaps acceleration of rupture across a discontinuity into the adjacent fault segment.

The rake angles for the high-frequency result (Fig. 2a) show more scatter than those for the low-frequency result (Fig. 2b). Numerical simulations of rupture on faults with non-uniform friction (i.e., with barriers to propagation in the form of areas of high fault strength) have produced irregular progression of the rupture front, resulting in a heterogeneous distribution of final slip vectors (Mikumo & Miyatake 1978). Dynamic rupture modeling assuming the slip-weakening law and isotropic friction has shown that rake rotation can occur if the initial shear stress level is low and the direction of stress is spatially variable (Guatteri & Spudich 1998). If we consider the geometric barriers we recognized at intersections of the XDF with other faults and at steps of the fault traces between fault segments as high-strength areas where the direction of shear stress is locally changed, the scatter or rotation of rake angle might be a result of a stress drop that exceeds the initial stress level, or of perturbations of stress at the barriers, and is consistent with field observations of fault exposures that show a mix of vertical and horizontal offsets, especially in areas near the XDF (Xu et al. 2009a; Yu et al. 2010). However, it is also possible that the HBP method cannot constrain rake angles on the basis of high-frequency signal intensity. Because the high-frequency waveforms contain more-complex and scattered phases than the low-frequency waveforms, the slight change of waveform amplitude responsible for variations of rake angle may not be resolved by the HBP method. For example, even when we fixed the rake angle of pre-calculated Greens function at 90° for all the source nodes, the results we obtained were similar to those obtained if rake angles in Greens functions were allowed to vary in the high-frequency analysis (Supporting Information Fig. S4). This instability raised from the high degree of freedom of the rake angle may explain the ghost image of the high-frequency signals shown at -200 km from the epicentre

at 30–50 s after the origin time shown in Fig. 3a. In contrast, the rake angles of the low-frequency result showed a smoother distribution than those of the high-frequency result, and were generally indicative of reverse faulting near the hypocentre, in the middle part of the SPF, and in the southern part of the SBF, and of horizontal slip near the intersections of the XDF with the SPF and SBF, and were consistent with the inverted slip models by using low-frequency waveforms (Yagi et al. 2012b; Hartzell et al. 2013).

Note that rake angles in Fig. 2 are annotated only for nodes with normalized signal intensities greater than 0.5 and that we constrained the range of values of rake angle (0° to 180°) according to the field observations (Xu et al. 2009a; Yu et al. 2010). However, histograms of the full range of rake angles (-180° to 180°) weighted according to single intensity show symmetric distributions with twin peaks at about -90° and 90° for both high- and low-frequency analyses (Supporting Information Fig. S5). Even if we searched the best rake angle associated with the highest signal intensity among the full set of rake angles, it was difficult to distinguish a unique rake angle in our methodology, because the polarity of the P-phase in the Greens function can be rotated by 180° by phase shifts when a narrow bandpass filter is applied. However, constraining the range of rake angles on the basis of the field observations allowed us to estimate the reliable rake angles that are comparable to those obtained by inversion modeling by using low-frequency waveforms.

Irregularity of rupture propagation is significant for earthquakes in fault systems that include geometric barriers. Such the rupture behavior, which was captured through the analysis of the teleseismic high-frequency waveforms and discussed in this study, may only be valid in a certain length scale around 10^0–10^1 km. However in finer scale, fault roughness (topographic variations of the fault surface) also generates high-frequency radiation, as quantitatively shown by dynamic rupture simulations (e.g. Dunham et al. 2011; Shi & Day 2013; Bruhat et al. 2016; Mai et al. 2017), and the roughness-induced irregularity of rupture propagation also plays a key role in high-frequecy wave radiation, although it is difficult to consider such the stochastic nature of the fault surface in this study due to the limited spatial resolution of the HBP method.

Considering the resonant frequencies of buildings that are partly consistent with the high-frequency band used in this study, our observation presented here may provide an input for assessment of risk associated with future earthquakes (e.g. Meng et al. 2012a) in populous inland areas where the likely locations of geometric discontinuities within their fault systems are pre-identified with geological and geomorphological efforts.

ACKNOWLEDGMENTS

We greatly acknowledge the editor Martin Mai, and the two anonymous reviewers for their critical

comments and constructive suggestions, which significantly improved and polished the manuscript. We thank Amato Kasahara, Hiroe Miyake, Lingsen Meng, Makoto Otsubo, Shiro Hirano, Shiqing Xu, and Wenyuan Fan for their valuable suggestions and comments during the early stage of this study. All the figures were generated with matplotlib (v2.0.2: http://doi.org/10.5281/zenodo.592536) (Hunter 2007) and ObsPy (1.0.3: http://doi.org/10.5281/zenodo.165134) (Beyreuther et al. 2010). This work was supported by Grant-in-aid for Japan Society for the Promotion of Science (JSPS) Research Fellow (JP16J00298) and JSPS Grants-in-aid for Scientific Research (JP16K05529 and JP16H01842). The IRISDMC provided access to the waveforms and related metadata from the seismic networks of II: IRIS/IDA Seismic Network (http://dx.doi.org/doi:10.7914/SN/II) and IU: Global Seismograph Network (GSN - IRIS/USGS) (GSN; http://dx.doi.org/doi:10.7914/SN/IU). All the data and materials to derive the conclusions of this study are archived on Github (https://github.com/rokuwaki).

REFERENCES

Aki, K., 1979. Characterization of barriers on an earthquake fault, *J. Geophys. Res.*, **84**(B11), 6140.

Aki, K. & Richards, P. G., 2002. *Quantitative seismology*.

Allmann, B. P. & Shearer, P. M., 2007. A High-Frequency Secondary Event During the 2004 Parkfield Earthquake, *Science*, **318**(5854), 1279–1283.

Bernard, P. & Madariaga, R., 1984. A new asymptotic method for the modeling of near-field accelerograms, *Bull. Seismol. Soc. Am.*, **74**(2), 539–557.

Beyreuther, M., Barsch, R., Krischer, L., Megies, T., Behr, Y., & Wassermann, J., 2010. ObsPy: A Python Toolbox for Seismology, *Seismol. Res. Lett.*, **81**(3), 530–533.

Bruhat, L., Fang, Z., & Dunham, E. M., 2016. Rupture complexity and the supershear transition on rough faults, *J. Geophys. Res. Solid Earth*, **121**(1), 210–224.

Burchfiel, B., Royden, L., van der Hilst, R., Hager, B., Chen, Z., King, R., Li, C., Lü, J., Yao, H., & Kirby, E., 2008. A geological and geophysical context for the Wenchuan earthquake of 12 May 2008, Sichuan, People's Republic of China, *GSA Today*, **18**(7), 4.

Clinton, J. F., 2006. The Observed Wander of the Natural Frequencies in a Structure, *Bull. Seismol. Soc. Am.*, **96**(1), 237–257.

Cocco, M. & Boatwright, J., 1993. The envelopes of acceleration time histories, *Bull. Seismol. Soc. Am.*, **83**(4), 1095–1114.

Danielson, J. & Gesch, D., 2011. Global Multi-resolution Terrain Elevation Data 2010(GMTED2010), *U.S. Geol. Surv. Open-File Rep. 20111073*, **2010**, 26.

Das, S. & Aki, K., 1977. Fault plane with barriers: A versatile earthquake model, *J. Geophys. Res.*, **82**(36), 5658–5670.

Dunham, E. M., Belanger, D., Cong, L., & Kozdon, J. E., 2011. Earthquake Ruptures with Strongly Rate-Weakening Friction and Off-Fault Plasticity, Part 2: Nonplanar Faults, *Bull. Seismol. Soc. Am.*, **101**(5), 2308–2322.

Fan, W. & Shearer, P. M., 2015. Detailed rupture imaging of the 25 April 2015 Nepal earthquake using teleseismic P waves, *Geophys. Res. Lett.*, **42**(14), 5744–5752.

Fan, W., Shearer, P. M., Ji, C., & Bassett, D., 2016. Multiple branching rupture of the 2009 Tonga-Samoa earthquake, *J. Geophys. Res. Solid Earth*, **121**(8), 5809–5827.

Fan, W., Bassett, D., Jiang, J., Shearer, P. M., & Ji, C., 2017. Rupture evolution of the 2006 Java tsunami earthquake and the possible role of splay faults, *Tectonophysics*, **721**(September), 143–150.

Fielding, E. J., Sladen, A., Li, Z., Avouac, J.-P., Burgmann, R., & Ryder, I., 2013. Kinematic fault slip evolution source models of the 2008 M7.9 Wenchuan earthquake in China from SAR interferometry, GPS and teleseismic analysis and implications for Longmen Shan tectonics, *Geophys. J. Int.*, **194**(2), 1138–1166.

Grandin, R., Vallée, M., Satriano, C., Lacassin, R., Klinger, Y., Simoes, M., & Bollinger, L., 2015. Rupture process of the M w = 7.9 2015 Gorkha earthquake (Nepal): Insights into Himalayan megathrust segmentation, *Geophys. Res. Lett.*, **42**(20), 8373–8382.

Guatteri, M. & Spudich, P., 1998. Coseismic temporal changes of slip direction: the effect of absolute stress on dynamic rupture, *Bull. Seismol. Soc. Am.*, **88**(3), 777–789.

Gusev, A. A. & Pavlov, V. M., 1991. Deconvolution of squared velocity waveform as applied to the study of a noncoherent short-period radiator in the earthquake source, *Pure Appl. Geophys. PAGEOPH*, **136**(2-3), 235–244.

Hartzell, S., Mendoza, C., RamirezGuzman, L., Zeng, Y., & Mooney, W., 2013. Rupture History of the 2008 M w 7.9 Wenchuan, China, Earthquake: Evaluation of Separate and Joint Inversions of Geodetic, Teleseismic, and StrongMotion Data, *Bull. Seismol. Soc. Am.*, **103**(1), 353–370.

Hashimoto, M., Enomoto, M., & Fukushima, Y., 2010. Coseismic Deformation from the 2008 Wenchuan, China, Earthquake Derived from ALOS/PALSAR Images, *Tectonophysics*, **491**(1-4), 59–71.

Hubbard, J. & Shaw, J. H., 2009. Uplift of the Longmen Shan and Tibetan plateau, and the 2008 Wenchuan (M = 7.9) earthquake, *Nature*, **458**(7235), 194–197.

Hubbard, J., Shaw, J. H., & Klinger, Y., 2010. Structural Setting of the 2008 Mw 7.9 Wenchuan, China, Earthquake, *Bull. Seismol. Soc. Am.*, **100**(5B), 2713–2735.

Hunter, J. D., 2007. Matplotlib: A 2D Graphics Environment, *Comput. Sci. Eng.*, **9**(3), 90–95.

Ide, S. & Aochi, H., 2005. Earthquakes as multiscale dynamic ruptures with heterogeneous fracture surface energy, *J. Geophys. Res. Solid Earth*, **110**(B11), 1–10.

Ishii, M., Shearer, P. M., Houston, H., & Vidale, J. E., 2005. Extent, duration and speed of the 2004 SumatraAndaman earthquake imaged by the Hi-Net array, *Nature*, **435**(June), 933–936.

Kakehi, Y. & Irikura, K., 1996. Estimation of high-frequency wave radiation areas on the fault plane by the envelope inversion of acceleration seismograms, *Geophys. J. Int.*, **125**(3), 892–900.

Kakehi, Y. & Irikura, K., 1997. High-frequency radiation process during earthquake faulting-envelope inversion of acceleration seismograms from the 1993 Hokkaido-Nansei-Oki, Japan, Earthquake, *Bull. Seismol. Soc. Am.*, **87**(4), 904–917.

Kakehi, Y., Irikura, K., & Hoshiba, M., 1996. Estimation of High-frequency Wave Radiation Areas on the Fault

Plane of the 1995 Hyogo-ken Nanbu Earthquake by the Envelope Inversion of Acceleration Seismograms., *J. Phys. Earth*, **44**(5), 505–517.

Kase, Y. & Day, S. M., 2006. Spontaneous rupture processes on a bending fault, *Geophys. Res. Lett.*, **33**(10), L10302.

Kennett, B. L. N., Engdahl, E. R., & Buland, R., 1995. Constraints on seismic velocities in the Earth from traveltimes, *Geophys. J. Int.*, **122**(1), 108–124.

Kikuchi, M. & Kanamori, H., 1991. Inversion of complex body wavesIII, *Bull. Seismol. Soc. Am.*, **81**(6), 2335–2350.

King, G. & Nábělek, J., 1985. Role of Fault Bends in the Initiation and Termination of Earthquake Rupture, *Science*, **228**(4702), 984–987.

Kohler, M. D., Heaton, T. H., & Bradford, S. C., 2007. Propagating Waves in the Steel, Moment-Frame Factor Building Recorded during Earthquakes, *Bull. Seismol. Soc. Am.*, **97**(4), 1334–1345.

Krüger, F. & Ohrnberger, M., 2005. Tracking the rupture of the Mw = 9.3 Sumatra earthquake over 1,150 km at teleseismic distance, *Nature*, **435**(June), 937–939.

Laske, G., Masters, G., Ma, Z., & Pasyanos, M., 2013. Update on CRUST1. 0A 1-degree global model of Earth's crust, *EGU Gen. Assem.*, **15**, 2658.

Liu-Zeng, J., Sun, J., Wang, P., Hudnut, K. W., Ji, C., Zhang, Z., Xu, Q., & Wen, L., 2012. Surface ruptures on the transverse Xiaoyudong fault: A significant segment boundary breached during the 2008 Wenchuan earthquake, China, *Tectonophysics*, **580**, 218–241.

Madariaga, R., 1977. High-frequency radiation from crack (stress drop) models of earthquake faulting, *Geophys. J. Int.*, **51**(3), 625–651.

Madariaga, R., Ampuero, J. P., & Adda-Bedia, M., 2006. Seismic radiation from simple models of earthquakes, in *Earthquakes Radiated Energy Phys. Faulting*, no. 1999, pp. 223–236.

Mai, P. M., Galis, M., Thingbaijam, K. K. S., Vyas, J. C., & Dunham, E. M., 2017. Accounting for Fault Roughness in Pseudo-Dynamic Ground-Motion Simulations, *Pure Appl. Geophys.*, **174**(9), 3419–3450.

Meng, L., Ampuero, J.-P., Sladen, A., & Rendon, H., 2012a. High-resolution backprojection at regional distance: Application to the Haiti M 7.0 earthquake and comparisons with finite source studies, *J. Geophys. Res. Solid Earth*, **117**(B4), n/a–n/a.

Meng, L., Ampuero, J.-P., Stock, J., Duputel, Z., Luo, Y., & Tsai, V. C., 2012b. Earthquake in a Maze: Compressional Rupture Branching During the 2012 Mw 8.6 Sumatra Earthquake, *Science*, **337**(6095), 724–726.

Michel, R. & Avouac, J.-P., 2002. Deformation due to the 17 August 1999 Izmit, Turkey, earthquake measured from SPOT images, *J. Geophys. Res. Solid Earth*, **107**(B4), ETG 2–1–ETG 2–6.

Mikumo, T. & Miyatake, T., 1978. Dynamical rupture process on a three-dimensional fault with non-uniform frictions and near-field seismic waves, *Geophys. J. Int.*, **54**(2), 417–438.

Muirhead, K. J. & Datt, R., 1976. The N-th root process applied to seismic array data, *Geophys. J. Int.*, **47**(1), 197–210.

Nakahara, H., 2008. Seismogram Envelope Inversion for HighFrequency Seismic Energy Radiation from ModeratetoLarge Earthquakes, in *Adv. Geophys.*, vol. 50, pp. 401–426.

Nakahara, H., Nishimura, T., Sato, H., & Ohtake, M., 1998. Seismogram envelope inversion for the spatial distribution of high-frequency energy radiation from the earthquake fault: Application to the 1994 far east off Sanriku earthquake, Japan, *J. Geophys. Res. Solid Earth*, **103**(B1), 855–867.

Oglesby, D., 2008. Rupture Termination and Jump on Parallel Offset Faults, *Bull. Seismol. Soc. Am.*, **98**(1), 440–447.

Oglesby, D. D. & Mai, P. M., 2012. Fault geometry, rupture dynamics and ground motion from potential earthquakes on the North Anatolian Fault under the Sea of Marmara, *Geophys. J. Int.*, **188**(3), 1071–1087.

Okuwaki, R., Yagi, Y., & Hirano, S., 2014. Relationship between High-frequency Radiation and Asperity Ruptures, Revealed by Hybrid Back-projection with a Non-planar Fault Model, *Sci. Rep.*, **4**(1), 7120.

Okuwaki, R., Yagi, Y., Aránguiz, R., González, J., & González, G., 2016. Rupture Process During the 2015 Illapel, Chile Earthquake: Zigzag-Along-Dip Rupture Episodes, *Pure Appl. Geophys.*, **173**(4), 1011–1020.

Sekiguchi, H., 2000. Fault Geometry at the Rupture Termination of the 1995 Hyogo-ken Nanbu Earthquake, *Bull. Seismol. Soc. Am.*, **90**(1), 117–133.

Shen, Z.-K., Sun, J., Zhang, P., Wan, Y., Wang, M., Bürgmann, R., Zeng, Y., Gan, W., Liao, H., & Wang, Q., 2009. Slip maxima at fault junctions and rupturing of barriers during the 2008 Wenchuan earthquake, *Nat. Geosci.*, **2**(10), 718–724.

Shi, Z. & Day, S. M., 2013. Rupture dynamics and ground motion from 3-D rough-fault simulations, *J. Geophys. Res. Solid Earth*, **118**(3), 1122–1141.

Snieder, R. & Şafak, E., 2006. Extracting the building response using seismic interferometry: Theory and application to the Millikan Library in Pasadena, California, *Bull. Seismol. Soc. Am.*, **96**(2), 586–598.

Spudich, P. & Frazer, L., 1984. Use of ray theory to calculate high-frequency radiation from earthquake sources having spatially variable rupture velocity and stress drop, *Bull. Seismol. Soc. Am.*, **74**(6), 2061–2082.

Uchide, T., Yao, H., & Shearer, P. M., 2013. Spatio-temporal distribution of fault slip and high-frequency radiation of the 2010 El Mayor-Cucapah, Mexico earthquake, *J. Geophys. Res. Solid Earth*, **118**(4), 1546–1555.

Walker, K. T., Ishii, M., & Shearer, P. M., 2005. Rupture details of the 28 March 2005 Sumatra M w 8.6 earthquake imaged with teleseismic P waves, *Geophys. Res. Lett.*, **32**(24), L24303.

Wan, Y., Shen, Z.-K., Bürgmann, R., Sun, J., & Wang, M., 2017. Fault geometry and slip distribution of the 2008 M w 7.9 Wenchuan, China earthquake, inferred from GPS and InSAR measurements, *Geophys. J. Int.*, **208**(2), 748–766.

Wesnousky, S. G., 2008. Displacement and Geometrical Characteristics of Earthquake Surface Ruptures: Issues and Implications for Seismic-Hazard Analysis and the Process of Earthquake Rupture, *Bull. Seismol. Soc. Am.*, **98**(4), 1609–1632.

Wright, T., Fielding, E., & Parsons, B., 2001. Triggered slip: Observations of the 17 August 1999 Izmit (Turkey) Earthquake using radar interferometry, *Geophys. Res. Lett.*, **28**(6), 1079–1082.

Xu, X., Wen, X., Yu, G., Chen, G., Klinger, Y., Hubbard, J., & Shaw, J., 2009a. Coseismic reverse- and oblique-slip surface faulting generated by the 2008 Mw 7.9 Wenchuan earthquake, China, *Geology*, **37**(6), 515–518.

Xu, Y., Koper, K. D., Sufri, O., Zhu, L., & Hutko, A. R., 2009b. Rupture imaging of the M w 7.9 12 May 2008 Wenchuan earthquake from back projection of teleseismic P waves, *Geochemistry, Geophys. Geosystems*, **10**(4), Q04006.

Yagi, Y. & Okuwaki, R., 2015. Integrated seismic source model of the 2015 Gorkha, Nepal, earthquake, *Geophys. Res. Lett.*, **42**(15), 6229–6235.

Yagi, Y., Nakao, A., & Kasahara, A., 2012a. Smooth and rapid slip near the Japan Trench during the 2011 Tohoku-oki earthquake revealed by a hybrid back-projection method, *Earth Planet. Sci. Lett.*, **355-356**, 94–101.

Yagi, Y., Nishimura, N., & Kasahara, A., 2012b. Source process of the 12 May 2008 Wenchuan, China, earthquake determined by waveform inversion of teleseismic body waves with a data covariance matrix, *Earth, Planets Sp.*, **64**(7), e13–e16.

Yu, G., Xu, X., Klinger, Y., Diao, G., Chen, G., Feng, X., Li, C., Zhu, A., Yuan, R., Guo, T., Sun, X., Tan, X., & An, Y., 2010. Fault-Scarp Features and Cascading-Rupture Model for the Mw 7.9 Wenchuan Earthquake, Eastern Tibetan Plateau, China, *Bull. Seismol. Soc. Am.*, **100**(5B), 2590–2614.

Zeng, Y., Aki, K., & Teng, T.-L., 1993. Mapping of the high-frequency source radiation for the Loma Prieta Earthquake, California, *J. Geophys. Res. Solid Earth*, **98**(B7), 11981–11993.

Zhang, H. & Ge, Z., 2010. Tracking the Rupture of the 2008 Wenchuan Earthquake by Using the Relative Back-Projection Method, *Bull. Seismol. Soc. Am.*, **100**(5B), 2551–2560.

SUPPORTING INFORMATION

Figure S1. Alternative results by using monoplane fault model.

Figure S2. Synthetic test of the HBP method.

Figure S3. Selected snapshots of Fig. 2.

Figure S4. Alternative results with fixed rake angle at 90.

Figure S5. Histograms of rake angles weighted by signal intensity.

Table S1. Near-source structure used to calculate Greens functions.